Journal of Japan Association for Earthquake Engineering, Vol. 20, No. 5, 2020

NUMERICAL SIMULATION FOR DETECTING INTERNAL VOID OF SEISMIC RUBBER BEARING

Yuuki NOSE[1], Kazuyuki IZUNO[2] and Yuma KAWASAKI[3]

[1] Graduate Student, Graduate School of Science and Engineering, Ritsumeikan University, Shiga, Japan, rd0048sv@ed.ritsumei.ac.jp
[2] Member, Professor, College of Science and Engineering, Ritsumeikan University, Shiga, Japan, izuno@se.ritsumei.ac.jp
[3] Member, Associate Professor, College of Science and Engineering, Ritsumeikan University, Shiga, Japan, yuma-k@fc.ritsumei.ac.jp

ABSTRACT: Deteriorated seismic rubber bearings exhibit inadequate isolation effects during earthquakes. Hence, the early detection of deterioration is necessary to provide safe, isolated structures. Deterioration of seismic rubber bearings usually starts from small internal voids in rubber. This study aimed to clarify the influence of a void in a seismic rubber bearing on elastic waves via numerical analyses. The results showed that a void affects the amplitude of the waves observed at a receiver if the void is located near the receiver.

Keywords: Seismic rubber bearing, Internal void, Nondestructive test, Wave propagation, Rational constrained interpolation profile scheme

1. INTRODUCTION

Elastomeric seismic isolation bearings have been commonly used in Japanese highway bridges, especially after the 1995 Great Hanshin-Awaji earthquake. Aging degradation problems of such bearings have become a critical problem. Some elastomeric bearings suffered severe damage owing to aging-related deterioration[1)]. As the isolation effects of deteriorated bearings during earthquakes are inadequate, early detection of deterioration is necessary to ensure the safety of isolated structures.

As an elastomeric bearing is covered with a protective rubber cover, internal deterioration cannot be detected unless the deterioration progresses to be seen via visual inspection. Further, after a huge earthquake, we must be able to distinguish whether we can continue to utilize the bearing or we should replace it with a new one. At present, visual inspection is the only effective measure available; however, it cannot be used to ascertain internal deterioration due to an earthquake. Hence, there is a need for a nondestructive technique to detect internal voids in seismic rubber bearings.

We conducted acoustic emission (AE) measurements to detect internal voids in rubber[2-5)]; however, the propagation paths of the elastic waves in rubber were not clear. Therefore, in this study, we aimed to clarify the propagation of elastic waves in rubber using numerical analyses. We verified our results by comparing them to the results of impact elastic wave tests. We also conducted numerical simulations using a model with an internal void and clarified the effects of a void in a rubber block on elastic wave propagation.

2. WAVE PROPAGATION SPEED IN RUBBER

2.1 Experimental setup

First, the wave propagation speed in rubber was verified through an impact elastic wave test. A specimen of G10 rubber specified by Japanese Industrial Standards (JIS) was used. The specimen was a rectangular parallelepiped of dimensions 150 × 150 × 150 mm, as shown in Figs. 1 and 2. Although actual seismic rubber bearings contain steel plates, we used a rubber block without steel plates as a basic study. We used AE sensors as receivers to observe the waves. As an AE sensor, a narrow-band sensor with a resonance frequency of 60 kHz was used. Eight receivers (Ch-1 to Ch-8) were installed on four sides of the specimen at identical heights (see Table 1 and Fig. 3). The waves were recorded at a sampling frequency of 1 MHz.

The same type of the AE sensor was also used as an actuator. A cosine wave (Eq. (1) and Fig.4) was generated using a function generator and sent to the actuator.

$$f(t) = \begin{cases} A\left\{1 - \cos\left(\frac{2\pi}{T}t\right)\right\} & (t \le T) \\ 0 & (t > T) \end{cases} \tag{1}$$

where t is time; A, amplitude; T, a period. We set $A = 2.5$ V and $T = 0.02$ ms in this study.

Table 1 Coordinates of actuator and receiver locations

Coordinates	Actuator	Ch-1	Ch-2	Ch-3	Ch-4	Ch-5	Ch-6	Ch-7	Ch-8
x (mm)	0	0	60	120	150	150	150	60	30
y (mm)	25	25	25	25	25	25	25	25	25
z (mm)	120	40	0	0	40	80	120	150	150

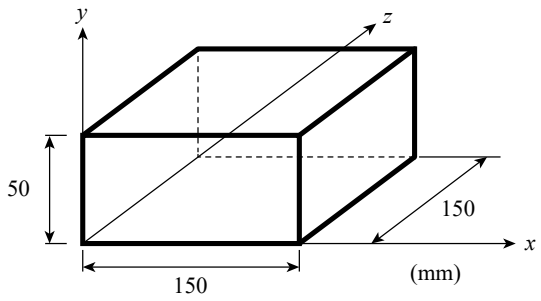

Fig. 1 Dimensions of specimen

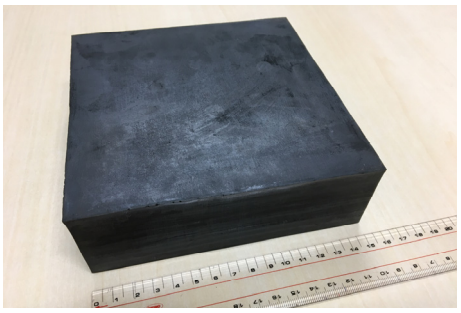

Fig. 2 Photo of specimen

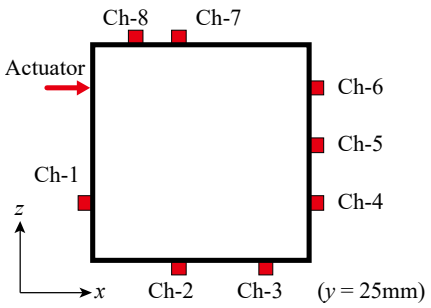

Fig. 3 Actuator and receivers layout

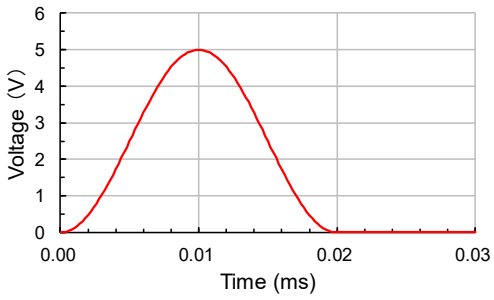

Fig. 4 Input wave

2.2 Obtained wave propagation speed

The elastic wave propagation speed was calculated from the time lag between the arrival time of the observed waves at receivers. Among the receivers, Ch-8, the one nearest to the actuator observed the wave first. Table 2 lists the time lag Δt between the arrival time at each receiver and that at Ch-8. Table 2 also lists the difference between the distance from the actuator to Ch-8 and that to the other receivers ΔL; the wave propagation speed $c_L = \Delta L/\Delta t$ can be calculated from these data. Though Ch-1 is the closest to the actuator, the waves arrived last at Ch-1 among all the receivers. As the AE sensor is sensitive to normally incident waves, we thought that the wave observed by Ch-1 was not the direct wave but the wave reflected from the opposite plane of the actuator.

We repeated five excitations under identical conditions and calculated the average (see Table 2). The variations between the measured arrival time lags for the five excitations were within 0.3 μs ($= 3 \times 10^{-4}$ ms), except for Ch-1 and Ch-6. The time lag between Ch-6 and Ch-8 showed a different value for 3.0 μs; however, the values for the other four times were almost the same. On the other hand, the values observed at Ch-1 varied much, with the maximum variation of 5.7 μs. Since small-amplitude reflected waves were observed at Ch-1, even a slight difference in the excitation resulted in a variation of the arrival time when the wave exceeded the threshold value for recording. However, the coefficient of variation for the propagation speed, as obtained from Table 2, was 0.078, which is considered sufficiently accurate for the following discussions.

The average propagation speed determined from these experiments was 1,604 m/s (Table 2). Further, we conducted an ultrasonic pulse velocity test and pencil lead break test using the same specimen and determined the propagation speed as 1,618 m/s and 1,630 m/s, respectively. Thus, we concluded that the elastic wave propagation speed in the rubber specimen was about 1,600 m/s.

Table 2 Observed wave speed from experiment

	Ch-1	Ch-2	Ch-3	Ch-4	Ch-5	Ch-6	Ch-7
Time lag Δt (ms)	0.185	0.052	0.073	0.078	0.069	0.066	0.018
Route difference ΔL (mm)	268.06	91.74	127.28	127.57	112.82	107.57	24.66
Wave speed $\Delta L / \Delta t$ (m/s)	1,447	1,751	1,735	1,642	1,635	1,620	1,398
Average speed c_L (m/s)				1,604		(CV	0.078)

3. NUMERICAL SIMULATION OF WAVE PROPAGATION

3.1 Numerical simulation method

The governing equations of three-dimensional (3D) elastodynamics in the stress-velocity formulation assuming linear and infinitesimal deformations are as follows:

$$\rho \partial_t V_x = \partial_x \sigma_{xx} + \partial_y \sigma_{xy} + \partial_z \sigma_{zx} \tag{2}$$
$$\rho \partial_t V_y = \partial_y \sigma_{yy} + \partial_z \sigma_{yz} + \partial_x \sigma_{xy} \tag{3}$$
$$\rho \partial_t V_z = \partial_z \sigma_{zz} + \partial_x \sigma_{zx} + \partial_y \sigma_{yz} \tag{4}$$
$$\partial_t \sigma_{xx} = (\lambda + 2\mu)\partial_x V_x + \lambda \partial_y V_y + \lambda \partial_z V_z \tag{5}$$
$$\partial_t \sigma_{yy} = \lambda \partial_x V_x + (\lambda + 2\mu)\partial_y V_y + \lambda \partial_z V_z \tag{6}$$
$$\partial_t \sigma_{zz} = \lambda \partial_x V_x + \lambda \partial_y V_y + (\lambda + 2\mu)\partial_z V_z \tag{7}$$
$$\partial_t \sigma_{yz} = \mu \partial_z V_y + \mu \partial_y V_z \tag{8}$$
$$\partial_t \sigma_{zx} = \mu \partial_x V_z + \mu \partial_z V_x \tag{9}$$
$$\partial_t \sigma_{xy} = \mu \partial_y V_x + \mu \partial_x V_y \tag{10}$$

where V is the particle velocity; σ, the stress; ρ, the density; ∂_t, the partial differential with respect to time t; further, λ and μ are Lame's constants; $\partial_x, \partial_y, \partial_z$ are the partial differentials with respect to space. The attenuation of the wave with distance is not considered here.

Using the fractional step technique, the 3D problem of Eqs. (2)–(10) can be calculated using one-dimensional (1D) equations. For example, the equations in x-direction are described as shown in Eqs. (11)–(14).

$$\partial_t h_1 + c_L \partial_x h_1 = 0,\ \partial_t h_2 - c_L \partial_x h_2 = 0 \tag{11}$$
$$\partial_t h_3 + c_T \partial_x h_3 = 0,\ \partial_t h_4 - c_T \partial_x h_4 = 0 \tag{12}$$
$$\partial_t h_5 + c_T \partial_x h_5 = 0,\ \partial_t h_6 - c_T \partial_x h_6 = 0 \tag{13}$$
$$\partial_t h_7 = 0,\ \partial_t h_8 = 0,\ \partial_t h_9 = 0 \tag{14}$$

where $h_1 = V_x - \frac{\sigma_{xx}}{c_L \rho},\ h_2 = V_x + \frac{\sigma_{xx}}{c_L \rho},\ h_3 = V_y - \frac{\sigma_{xy}}{c_T \rho},\ h_4 = V_y + \frac{\sigma_{xy}}{c_T \rho},\ h_5 = V_z - \frac{\sigma_{zx}}{c_T \rho},\ h_6 = V_z + \frac{\sigma_{zx}}{c_T \rho},$ $h_7 = \sigma_{yy} - \frac{\lambda}{\lambda+2\mu}\sigma_{xx},\ h_8 = \sigma_{zz} - \frac{\lambda}{\lambda+2\mu}\sigma_{xx},\ h_9 = \sigma_{yz},\ c_L = \sqrt{\frac{\lambda+2\mu}{\rho}},\ c_T = \sqrt{\frac{\mu}{\rho}}$.

Eq. (14) shows that h_7, h_8 and h_9 do not vary with time. Eqs. (11)–(13) are 1D advection equations for longitudinal wave speed c_L and transverse wave speed c_T.

In this study, these advection equations are solved using the rational constrained interpolation profile (RCIP) scheme[6]. In this method, the spatial derivative of the variables is assumed to propagate according to the advection equations. We obtained h_i and g_i, the spatial derivative of h_i (i = 1, 2, ..., 6) in the x-direction, by the RCIP method. As the space derivatives in the y- and z-directions of h_i could not be obtained from the advection equations in the x-direction, $\partial_y h_i$ and $\partial_z h_i$ were calculated from g_i by the central difference method[7]. Then, these schemes were applied to the y- and z-directions.

We modeled the specimen used in the experiment as a rectangular parallelepiped with sides parallel to the coordinate axes, as shown in Fig. 1. Since the boundaries of this model were orthogonal to the axes, the boundary conditions at free surfaces were satisfied by assuming appropriate virtual incoming waves from outside the domain[8]. The boundary conditions for the x-direction are as follows:

$$h_1 = h_2,\ h_3 = h_4,\ h_5 = h_6 \tag{15}$$
$$\partial_x h_1 = -\partial_x h_2,\ \partial_x h_3 = -\partial_x h_4,\ \partial_x h_5 = -\partial_x h_6 \tag{16}$$
$$\partial_y h_1 = \partial_y h_2,\ \ \partial_y h_3 = \partial_y h_4,\ \partial_y h_5 = \partial_y h_6 \tag{17}$$
$$\partial_z h_1 = \partial_z h_2,\ \partial_z h_3 = \partial_z h_4,\ \partial_z h_5 = \partial_z h_6 \tag{18}$$

The external force term of Eq. (1) was used in the fractional step equation for the x-direction derived from Eq. (2). To improve the numerical stability, a distributed loading as expressed in Eq. (19) was adopted.

$$p(r) = \begin{cases} \frac{1}{2}\left\{1 + \cos\left(\frac{2\pi}{d} r\right)\right\} & (r \le d/2) \\ 0 & (r > d/2) \end{cases} \tag{19}$$

where $r = \sqrt{(y - y_0)^2 + (z - z_0)^2}$ is the distance from the excitation point $(x, y, z) = (x_0, y_0, z_0)$ in the loading plane $(x, y, z) = (0, y, z)$; d = 10 mm because the installation surface of the receiver used in the experiment was a circle with 10 mm diameter. Figure 5 shows the load distribution near the excitation point $(x, y, z) = (0, 25{,}125)$ mm on the z-axis. Thus, h_1 in Eq. (11) was transformed into Eq. (20) on considering the loading. We assumed the coefficient of Eq. (1) as $A = 1$ N in the following simulations.

$$\partial_t h_1 + c_L \partial_x h_1 = f(t) p(r) / \rho \tag{20}$$

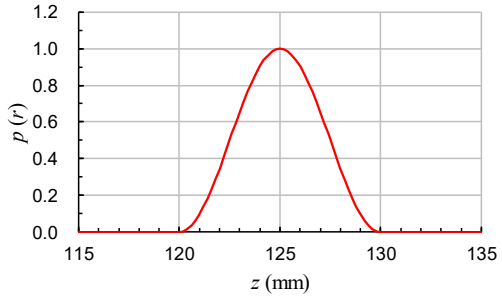

Fig. 5 Distributed load

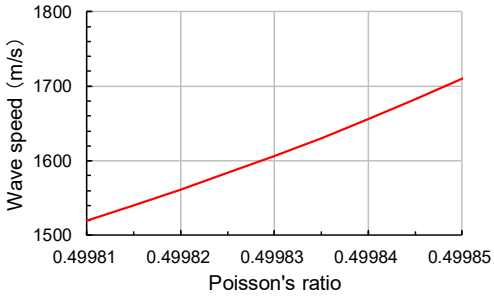

Fig. 6 Relation between Poisson's ratio and wave speed

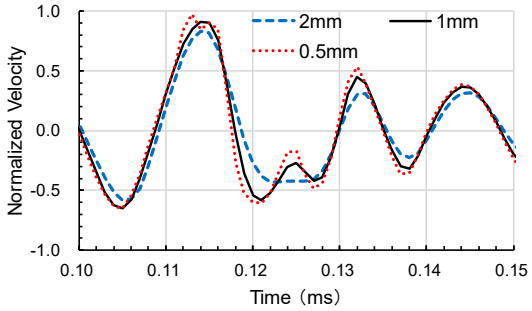

Fig. 7 Effect of mesh size on particle velocity

3.2 Analytical model

A rectangular parallelepiped identical in size to the experimental specimen was used as the numerical model. The excitation point and the observation points were set at the same points as the actuator and receivers in the experiment. Since the experimental specimen was G10 rubber as specified by JIS, the elastic shear modulus in the model was set $G = 1.0$ MPa. The density was calculated as $\rho = 1{,}140$ kg/m^3 from the weight of the experimental specimen (1.28 kg). The Poisson's ratio ν of rubber is slightly less than 0.5; however, it was not verified in the experiment. We estimated the Poisson's ratio of the specimen from the propagation speed we obtained in section 2.2. The longitudinal speed c_L and the transverse speed c_T are expressed as shown in Eq. (21) using G, ρ and ν.

$$c_L = \sqrt{\frac{2G}{\rho}\frac{1-\nu}{1-2\nu}} \quad , \quad c_T = \sqrt{\frac{G}{\rho}} \tag{21}$$

Because of the term $(1-2\nu)$ in the denominator of c_L in Eq. (21), c_L changes significantly if ν approaches 0.5. The relation between c_L and Poisson's ratio ν is shown in Fig. 6. As we estimated c_L as 1600 m/s (see section 2.2), $\nu = 0.49983$ was assumed in the simulations (Fig. 6). However, the transverse speed c_T in Eq. (21) is independent of the Poisson's ratio and is about 30 m/s, which is less than 1/50 of c_L.

Next, to identify a suitable grid size for RCIP simulations, we used models with 2, 1 and 0.5 mm cubic grids. The computation time using Intel Xeon E3-1245 Linux PC was about 4 min for the 2-mm grid model, about 1 h for the 1-mm grid model, and about 1 day for the 0.5-mm grid model. Figure 7 shows the particle velocity at Ch-6 where the observed values were the largest among all the observation points. The lines are normalized by the maximum value of the 0.5-mm grid model. The lines of the 2-mm grid model differed from those of the other models, with the maximum value 15% smaller than that of the 0.5-mm grid model. On the other hand, the lines for the 0.5-mm grid model and 1-mm grid model were similar, with the maximum difference of only 6%. Hence, we used the 1-mm grid model in this study.

We set the time increment to $\Delta t = 0.2$ μs so that the Courant number was about 0.5 and used the

moving average to obtain data every 1 μs. Assuming that the observed data in the experiment was proportional to the acceleration, the calculated particle velocity was numerically differentiated to obtain the acceleration. As the installation cross section of the receiver in the experiment was a circle with 10 mm diameter, the acceleration in a circular area around the observation point was averaged.

3.3 Results and discussions

The unit of the analytical data is meter per second squared, while that of the experimental data is volt. To compare the analytical results with the experimental values, each value was normalized by the maximum value at Ch-6, which is the nearest observation point from the excitation point. Further, although the relative arrival time at each receiver was clear, in the experiment, the time elapsed since the excitation was unknown. Then, we adjusted the arrival time of Ch-6 between the experiment and numerical simulation and set the abscissa as the time since excitation in the numerical simulation (see Figs. 8–15). Assuming that the observed waves in the experiment were orthogonal to the planes where the receivers were installed, we used the x-direction values in the numerical simulation of the points in the y-z plane: Ch-1, 4, 5 and 6, and the z-direction values in the numerical simulation of those in the x-y plane: Ch-2, 3, 7 and 8. Figures 8–15 compare the normalized wave-time histories between the experiment and numerical simulation. Note that Fig. 8 shows the duration from 0.1 to 0.3 ms, while the others show the results for time duration from 0 to 0.2 ms.

Because both traveling waves and backward waves are present, the wave repeatedly crosses the excitation points as the excited wave propagates. Thus, although we used only 1 cosine wave cycle as shown in Fig. 1, many cycles of wave actually propagated from a point. Further, the receiver also observed waves reflected from the boundaries. Hence, many cycles of waves are seen in Figs. 8–15.

Figures 16 and 17 show snapshots of the spatial distribution of the absolute particle velocities in a plane orthogonal to the y-axis at the same height as that of the receivers, i.e., $y = 25$ mm. Figures 16 and 17 show the wave distribution at 0.05 and 0.1 ms, respectively, since excitation. In the figures, red color indicates the regions with high velocities. Red areas are seen around the excitation point even after 0.1 ms in the figures because of the effect of continuous loading of the nearly incompressible material and also because of the slow transverse wave, which propagates at speeds of less than 1/50 of the longitudinal wave speed. Therefore, the numerical simulation was less accurate near the excitation point.

Figure 16 shows the distribution when the first wave arrived Ch-7. A wavefront of the reflected wave from the upper side of the figure ($z = 150$ mm) is seen between Ch-7 and Ch-8. Thus, both a direct and reflected wave arrived at Ch-7 and Ch-8 almost simultaneously. Figure 17 shows the distribution just before the first wave arrived at Ch-3 and Ch-4. The interference waves between the direct and reflected waves is observed near Ch-6. No waves are observed near Ch-7 and Ch-8 (blue region) in this figure; however, the experimental results shown in Figs. 14 and 15 indicate that these receivers still received waves at this time.

As the incident angle of the direct wave reaching Ch-4 and Ch-5 are far from orthogonal, as shown in Fig. 17, the amplitude of the x-direction component of the wave at Ch-4 and Ch-5 was smaller than that at Ch-6 (Figs. 11–13). Assuming incident angle θ as shown in Fig. 18, relation between $\cos\theta$ and the maximum amplitude normalized by the maximum value of Ch-6 is shown in Fig. 19. This figure shows that there are large variations in the experimental values and in the analytical values. Thus, the incident angle had a small effect on the wave amplitude at the receivers.

A comparison of the results of the numerical simulations and experiment shows that the numerical simulation is less accurate for Ch-1 and Ch-8 located near the excitation point (Figs. 8 and 15). Further, the first wave arriving at Ch-2 and Ch-3 (Figs. 9 and 10) was well simulated and in good agreement with the experimental results; however, after the second wave, the phase of the wave differed from that in the experiment. With regard to Ch-4, 5, 6 and 7, phase differences existed since the latter half of the first wave. To explain these behaviors, we employed spectrograms using Gabor wavelets of the experimental observed wave and numerically simulated wave at Ch-6. These spectrograms are shown in Figs. 20 and 21. The both figures show that waves with the predominant frequency of 60 kHz arrived 0.1 ms after the excitation. Although the experimental observed wave (Fig. 20) has a wide predominant

frequency range of 50–80 kHz, the numerically simulated wave (Fig. 21) has a narrower predominant frequency range. This difference caused the phase difference between the experimental and numerically simulated waves.

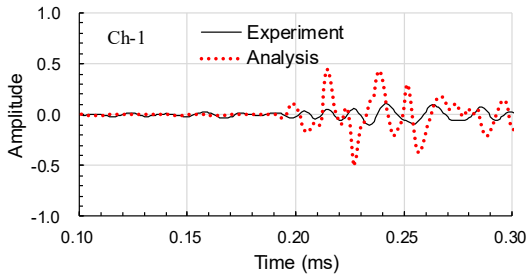

Fig. 8 Comparison of velocity-time histories at Ch-1 between experiment and analysis

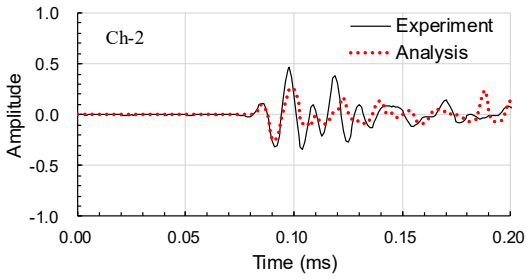

Fig. 9 Comparison of velocity-time histories at Ch-2 between experiment and analysis

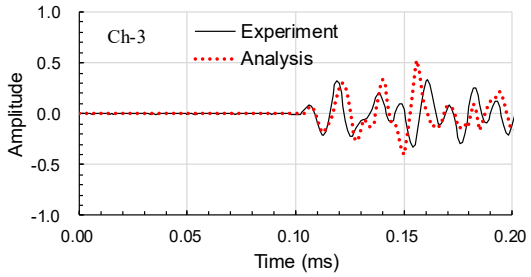

Fig. 10 Comparison of velocity-time histories at Ch-3 between experiment and analysis

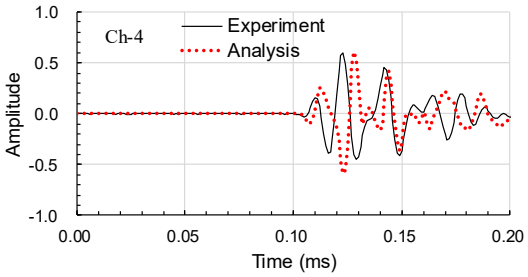

Fig. 11 Comparison of velocity-time histories at Ch-4 between experiment and analysis

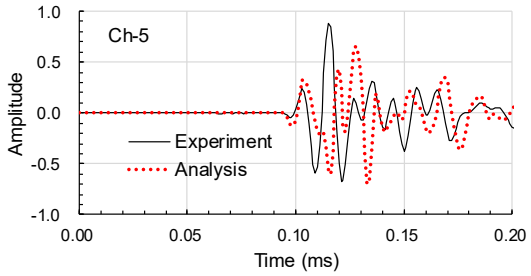

Fig. 12 Comparison of velocity-time histories at Ch-5 between experiment and analysis

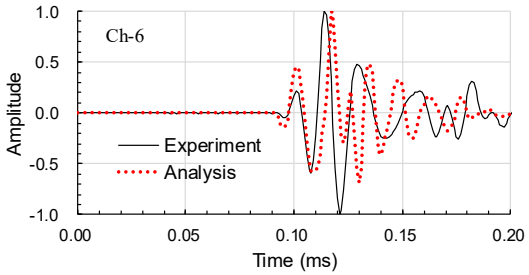

Fig. 13 Comparison of velocity-time histories at Ch-6 between experiment and analysis

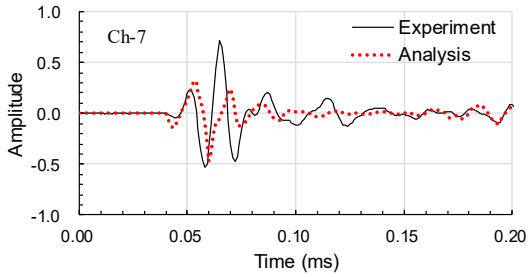

Fig. 14 Comparison of velocity-time histories at Ch-7 between experiment and analysis

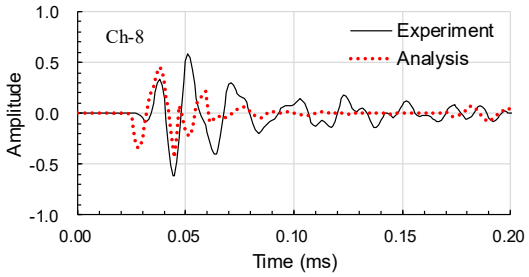

Fig. 15 Comparison of velocity-time histories at Ch-8 between experiment and analysis

The experimental wave had more high-frequency components than the numerical simulated wave for all receivers. The two reasons for this difference are (1) the effect of the difference between the spatial distribution of excitation wave as shown in Eq. (19) and Fig. 5; (2) the difference between the excitation—the digital input to discrete points in the numerical simulation against the analog input to a continuous plane in the experiment.

Further, the spectrogram for the experimental waves (Fig. 20) showed that waves with frequencies higher than 40 kHz attenuated sooner than those with lower frequencies. In other words, the attenuation characteristics showed frequency dependency. In contrast, the spectrogram for numerical simulation (Fig. 21) showed that waves with a dominant frequency around 60 kHz continued longer than the corresponding experimental waves. As the second and later waves that arrived included the waves reflected from various boundaries, the flatness and squareness of the specimen affected wave reflection at the boundaries. The specimen used in the experiment was cut from a 50-mm-thick rubber plate with

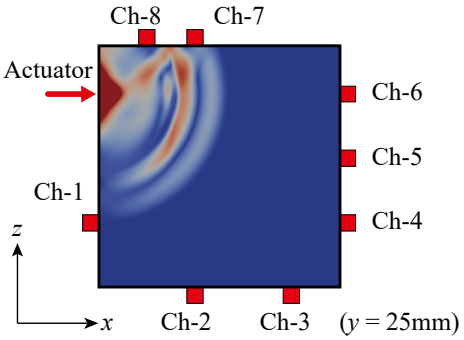

Fig. 16 Wave propagation situation after 0.05 ms

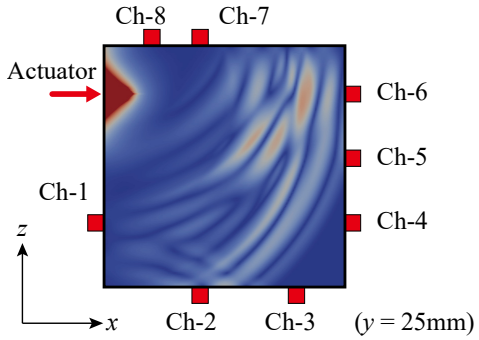

Fig. 17 Wave propagation situation after 0.1 ms

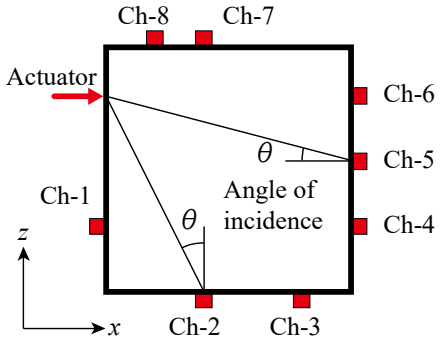

Fig. 18 Angle of incidence to receivers

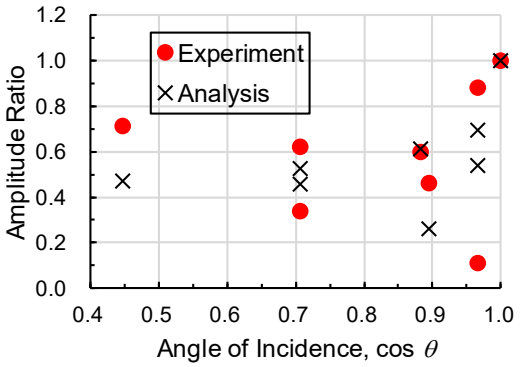

Fig. 19 Relation between amplitude and angle of incidence

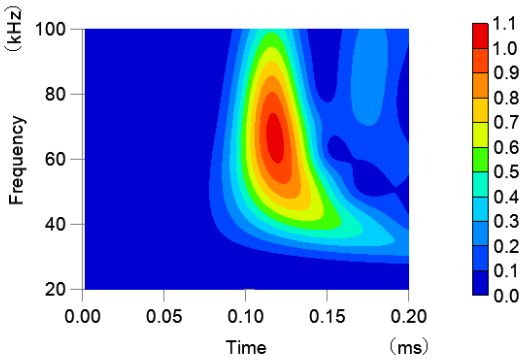

Fig. 20 Spectrogram of observed data at Ch-6

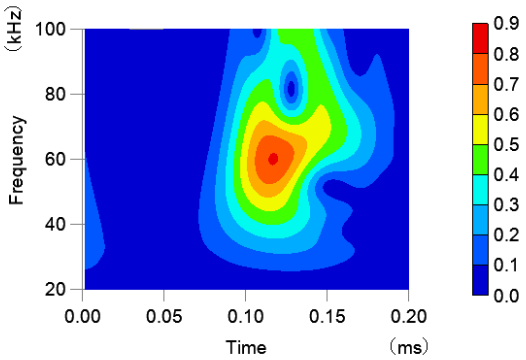

Fig. 21 Spectrogram of calculated data at Ch-6

dimensions 150 (length) × 150 (width) mm. Therefore, the flatness and squareness in x-y and y-z planes were imperfect. Further, there existed differences in the boundary condition of the bottom plane. The experiment was conducted after placing the specimen on a table, whereas in the numerical simulation, all planes were assumed surrounded by air in equilibrium. These conditions also resulted in the differences between the spectrograms of the experiment and numerical simulation.

The analytically obtained wave at Ch-1 (Fig. 8) had greater amplitude than the experimental wave. As mentioned above, at Ch-1, the observed wave was not the direct wave but the wave reflected from the opposite plane. Thus, the observed wave at Ch-1 traveled much longer than the observed waves at other points. As the amplitude of the experimentally observed wave was small, we expect that the wave attenuated with distance. Although in this study, we did not consider wave attenuation, this factor should be considered to simulate experimental results precisely.

The numerical accuracy of the first-arrived wave is low for Ch-8 (Fig. 15). This point is the nearest to the excitation point. We consider that this point was the most affected by the aforementioned difference in excitation between the experiment and numerical simulation.

4. EFFECT OF INTERNAL VOID ON WAVE PROPAGATION

4.1 Assumed location of a void

The effect of an internal void in rubber on wave propagation is discussed in this section. We used the same aforementioned analytical model and assumed an internal void in it. The deterioration of rubber bearings usually occurs from a crack in the rubber. Therefore, we assumed a void with a crack-like form as a thin rectangular parallelepiped. The main purpose of this simulation was to clarify the reflection phenomena of the propagating wave at the interface of the void. Hence, a rather large void of (x, y, z) = (10, 2, 10) mm was assumed.

We assumed three locations for the void as shown in Fig. 22. In Cases 1 and 2, a void is located near Ch-6, while in Case 3, the void is located at the center of the model. The void is set at the same height as the excitation and observation points (y = 25 mm) in Cases 1 and 3; it is set near the bottom (y = 10 mm) in Case 2.

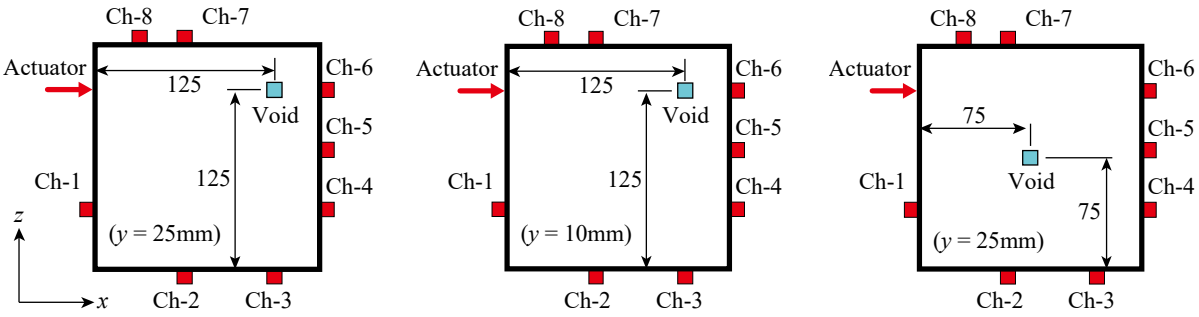

(a) Case 1 (b) Case 2 (c) Case 3

Fig. 22 Assumed void location

4.2 Results and discussions

Figure 23 shows the maximum acceleration at each receiver point normalized by that in the case without any voids. We found that for Cases 1 and 2, most of the points showed values 10–20% larger than the value for the case without voids. In contrast, for Case 3, the values were smaller by 10% for some points; however, the effect of the void was less compared to Cases 1 and 2.

Figures 24 and 25 show the acceleration-time histories at Ch-4 and Ch-6 normalized by the maximum value at Ch-6 without any voids. Although the amplitude changed because of the presence of

the void, the phase changed only slightly. The amplitude at Ch-4 (Fig. 24) changed at time 0.12–0.13 ms, when the amplitude was the maximum. On the other hand, the amplitude at Ch-5 (Fig. 25) changed after the maximum amplitude (0.12–0.14 ms) because of the waves reflected from the interface of the void and the boundary of the model.

The maximum amplitude distribution at the side opposite to the actuator is shown in Figs. 26–29. Case 1 in Fig. 27 shows larger values than the case without any voids (Fig. 26) for Ch-5 and Ch-6 because of the waves reflected from the side of the void. Case 2 in Fig. 28 also shows larger values at similar locations because of the waves reflected from top of the void.

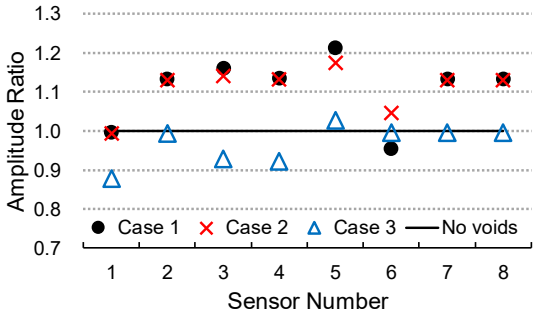

Fig. 23 Amplitude ratio of model with void to that without voids

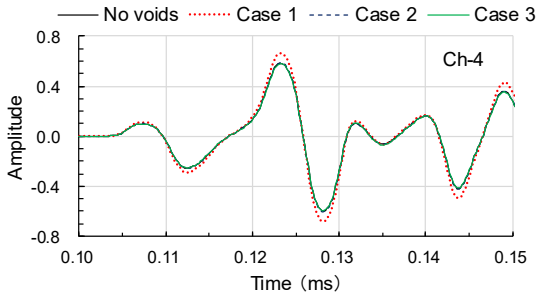

Fig. 24 Comparison between velocity-time histories at Ch-4 with and without void

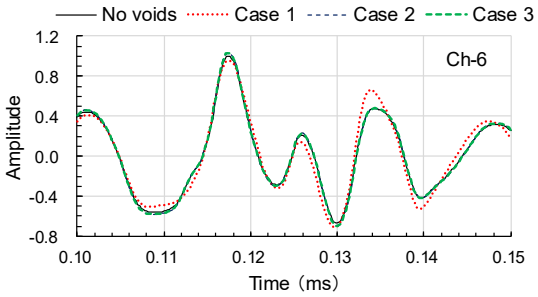

Fig. 25 Comparison between velocity-time histories at Ch-6 with and without void

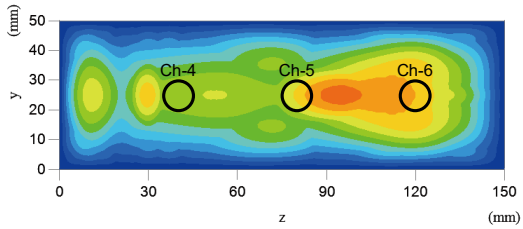

Fig. 26 Contour map of maximum amplitude for model without voids

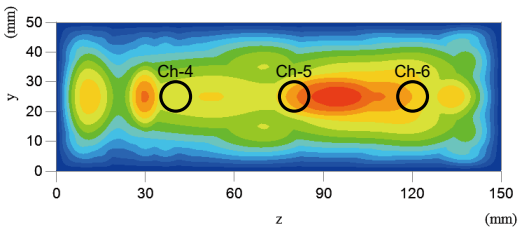

Fig. 27 Contour map of maximum amplitude for Case 1

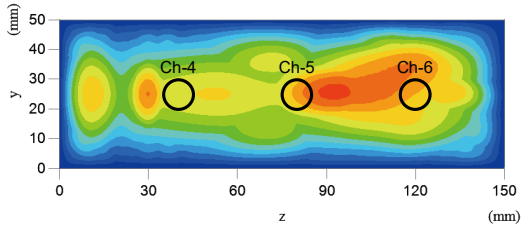

Fig. 28 Contour map of maximum amplitude for Case 2

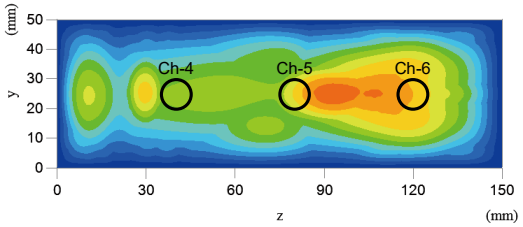

Fig. 29 Contour map of maximum amplitude for Case 3

Case 3 in Fig. 29 shows smaller values for Ch-4 and Ch-5 than those seen in Fig. 26 because the void is located along the path from the actuator to the opposite plane; however, the difference is small. Therefore, it is hard to detect internal voids located far from the receivers.

Thus, if values for a case without any voids are known, we can detect the existence of internal voids from the change in the amplitude. However, the layout of the receivers should be considered carefully because the influence zone of a void is small.

5. CONCLUSIONS

The aim of this study was to detect internal voids in seismic rubber bearings by a nondestructive method. We conducted an impact elastic wave test using a rubber specimen and numerical simulation of wave propagation using the RCIP method. The main conclusions were as follows:

1) From the experiment, the longitudinal wave propagation speed was estimated at about 1,600 m/s.
2) Waves with frequencies around 60 kHz were observed in the experiments and numerical analyses. However, waves with frequencies higher than 40 kHz attenuated faster in the experiment than in the numerical analyses, and attenuation characteristics showed frequency dependency.
3) Although the precision of the numerically obtained waves near the actuator was low, the amplitudes of the first-arrived waves at other locations were in good agreement with those in the experimental results.
4) The numerical analysis results showed that internal voids can be detected if the wave propagation characteristics for a case with no voids are known. However, as area of influence of a void is small, the receiver layout should be considered carefully.

ACKNOWLEDGMENT

The authors would like to thank Rubber Bearing Association for providing rubber bearing test specimens. We also thank Mr. Naoto Teramura of JIP Techno Science Corporation, a former graduate student of Ritsumeikan University, for his help in the ultrasonic tests and the pencil lead break tests.

REFERENCES

1) Hayashi, K., Adachi, Y., Komoto, K., Yatsumoto, H., Igarashi, A., Dang, J. and Higashide, T.: Experimental Verification for Remaining Performance of Lead Rubber Bearings with Aging Deterioration, *Journal of Japan Society of Civil Engineers*, Ser. A1, Vol. 70, No. 4, pp. 1032–1042, 2014. (in Japanese)
2) Kawasaki, Y., Teramura, N., Izuno, K. and Okada, S.: Using Acoustic Emissions to Assess Damage to Laminated Rubber Bearings, *Journal of Japan Society of Civil Engineers*, Ser. A1, Vol. 71, No. 2, pp. 244–254, 2015. (in Japanese)
3) Teramura, N., Kawasaki, Y. and Izuno, K.: Health Monitoring of Laminated Rubber Bearings by Acoustic Emission, *Journal of Japan Association for Earthquake Engineering*, Vol. 15, No. 7, pp. 7_335–7_342, 2015. (in Japanese)
4) Kawasaki, Y., Tanaka, A., Teramura, N., Ueda, K. and Izuno, K.: Accuracy Evaluation Test to Detect Peeling Sound Inside Rubber by AE Method, *Journal of Japan Society of Civil Engineers*, Ser. A1, Vol. 74, No. 2, pp. 241–250, 2018. (in Japanese)
5) Tanaka, A., Kawasaki, Y., Ueda, K. and Izuno, K.: Influence of Cyclic Shear Deformation on AE Characteristics of Laminated Rubber Bearing, *Journal of Japan Society of Civil Engineers*, Ser. A1, Vol. 74, No. 4, pp. I_481–I_489, 2018. (in Japanese)
6) Xiao, F., Yabe, T. and Ito, T.: Constructing oscillation preventing scheme for advection equation by rational function, *Computer Physics Communications*, Vol. 93, pp. 1–12, 1996.
7) Nakamura, T. and Yabe, T.: Cubic Interpolate Propagation Scheme for Solving the Hyper-

Dimensional Vlasov-Poisson Equation in Phase Space, *Computer Physics Communications*, Vol. 120, pp. 122–154, 1999.
8) Saito, J.: An Application of the CIP Method to Elastodynamics, *Journal of Applied Mechanics: JSCE*, Vol. 12, pp. 135–137, 2009. (in Japanese)

(Original Japanese Paper Published: September, 2019)
(English Version Submitted: January 18, 2020)
(English Version Accepted: February 19, 2020)